npj | 2D materials and applications

Article

Published in partnership with FCT NOVA with the support of E-MRS

https://doi.org/10.1038/s41699-026-00745-7

DC-operated near-infrared light emitting diode based on MOCVD-grown WSe_2 monolayers

Check for updates

Tobiloba Grace Fabunmi[1], Melike Seda Kartal[1], Songyao Tang[2], Henrik Myja[1], Nicole Stracke[1], Yibing Wang[2], Yingfang Ding[2], Michael Heuken[2,3], Holger Kalisch[2], Andrei Vescan[2], Tilmar Kümmell[1] ✉ & Gerd Bacher[1]

Monolayer transition metal dichalcogenides (TMDC) combine huge oscillator strength with naturally terminated surfaces, enabling optoelectronic devices on various platforms. Despite numerous efforts to integrate 2D materials in light-emitting devices, a scalable direct current (DC) driven near-infrared 2D material-based (NIR) emitter has not been reported yet. In this work, a large-area, DC-operated NIR light-emitting device based on WSe_2 monolayers grown by metal-organic chemical vapor deposition (MOCVD) is presented. Our scalable device architecture enables a diode-like *I–V* curve with a rectifying ratio exceeding 20 and a turn-on voltage of ~1.5 V, indicating excellent electrical performance. NIR electroluminescence at 778 nm is observed at 1.5 V, along with a radiance of ~2 μW cm^{-2} sr^{-1} at 5 V under DC operation.

Near-infrared (NIR) light sources have attracted increasing research attention for applications, e.g., in biomedical imaging, agricultural diagnostics of plant composites, and night vision[1–3]. NIR light sources with wavelengths below 1000 nm are increasingly preferred, particularly for diagnostic imaging of living tissues and cells[4]. This is due to the possibility of controlling penetration depth and protecting the target surface, such as plant cells, from excessive damage[5]. Inorganic semiconductor-based NIR photon sources are preferable for their long-term functionality and versatile adaptability to different environments or conditions. Various inorganic material systems, such as colloidal quantum dots (QDs) based on InAs[6] or PbS[7], respectively, as well as epitaxially grown III-V semiconductors, mainly based on (In,Ga)As[8–10], have been explored for the development of NIR light-emitting devices (LEDs). However, colloidal QDs generally face challenges of low stability, exciton quenching, and fast degradation[11], while the epitaxially grown semiconductors strongly depend on their lattice matching with the growth substrate[12]. Therefore, semiconductor-based NIR emitters that are able to overcome those challenges are in high demand.

Two-dimensional materials, such as transition metal dichalcogenides (TMDCs), have become highly attractive candidates for this purpose. Their van der Waals (vdW)-layered structure and monolayer nature make them flexible and compatible with various platforms, rendering lattice mismatch irrelevant for device integration[13–15]. Their strong exciton binding energy and high oscillator strength make them potentially bright emitters, and their direct band gap in the case of a monolayer (ML) indicates strong prospects for radiative recombination[16]. TMDCs exhibit distinct quantum confinement effects and wavelength tunability that arise from the combinations of different metal and chalcogen atoms. For example, tungsten diselenide (WSe_2) and molybdenum diselenide ($MoSe_2$) are possible NIR emitters with emission wavelengths in the 700–800 nm range[17]. In the past decade, WSe_2-based NIR LEDs have been explored using mechanically exfoliated flakes for high device performance[18,19] as well as flakes grown by chemical vapor deposition (CVD)[20]. Even heterostructures using a waveguide-integrated structure[19,21], or horizontal architectures based on a tunnelling transistor design[18,22], have been reported. Recently, Lien et al.[23] presented a large-area CVD-based WSe_2 NIR LED employing a capacitor architecture under alternating-current (AC) operation. A common challenge that still requires attention is the scalability and direct current (DC) operation of TMDC NIR LEDs, which are essential for uniform and accurate control in diagnostic applications.

In this work, we demonstrate the integration of large-scale MOCVD-grown WSe_2 monolayers into a scalable vertical architecture to realize NIR LEDs that operate under DC. We use a combination of poly (3,4-ethylenedioxythiophene): poly (styrene sulfonate) (PEDOT: PSS) and poly[N, N ′-bis(butylphenyl)-N,N(phenyl)benzidine] (poly-TPD) on glass as the anode, and magnesium-doped zinc oxide (MgZnO) with an aluminium contact as the cathode. WSe_2 monolayers grown on a 2-inch *c*-plane sapphire wafer in a commercial AIXTRON MOCVD reactor were transferred via a water-assisted method, and afterwards sandwiched between the anode and cathode, with an emitting area of 6 mm^2 as defined by the metal

[1]Werkstoffe der Elektrotechnik & CENIDE, University of Duisburg-Essen, Duisburg, Germany. [2]Compound Semiconductor Technology, RWTH Aachen University, Aachen, Germany. [3]AIXTRON SE, Herzogenrath, Germany. ✉e-mail: tilmar.kuemmell@uni-due.de

contacts. A near-infrared electroluminescence (EL) at 778 nm was observed at 1.5 V, with a radiance of 2 μW/sr/cm^2 at 5 V under DC operation.

Results

Fabrication and homogeneity of WSe_2 monolayers

To fabricate a scalable WSe_2 NIR LED, a large-area, coalesced WSe_2 monolayer is required. Therefore, WSe_2 was synthesized on a 2-inch *c*-plane sapphire ((0001) oriented with a 0.2° offcut toward the m-plane) wafer in a commercial AIXTRON close-coupled showerhead (CCS) MOCVD reactor using tungsten hexacarbonyl ($W(CO)_6$) and di-iso-propyl selenide $C_6H_{14}Se$ (DiPSe) as W and Se precursors, respectively. Details of the growth processes are provided in the methods, and further information on process development has been reported elsewhere[24]. As schematically illustrated in Fig. 1a, typical PL signals were collected from various regions across the wafer. Each spectrum represents a statistical average of 4225 individual spectra, acquired over a 95 ×95 μm^2 area with a spatial resolution of 1.5 μm. The luminescence wavelength slightly varies between 747 and 750.8 nm, depending on the position on the wafer. The spectral shape is consistent across this range, and no additional spectral features are observed beyond 800 nm.

To further investigate the homogeneity of the PL signal, a highly spatially resolved representative PL map corresponding to the 95 ×95 μm^2 area was analyzed. The images are shown in Fig. 1b (intensity map) and c (peak energy map). Obviously, a PL signal that can be assigned to the direct bandgap[25] of WSe_2 monolayers is observed at every position, showing high uniformity of a strongly coalescent monolayer over the whole area. The peak PL intensity exhibits a standard deviation of approximately 10% within the given square area. The spatially resolved PL peak position map shown in Fig. 1c confirms the full WSe_2 coverage in the given area with a mean emission wavelength derived as 749 ± 2 nm. This indicates that the spectral position of the PL across this area does not vary strongly. To further confirm the homogeneity of the monolayers over a large area, multiple ~95 μm^2 area PL maps were obtained from various segments of the wafer (see Supplementary Fig. S1). Each map has a spatial resolution of 1.5 μm. The PL map of

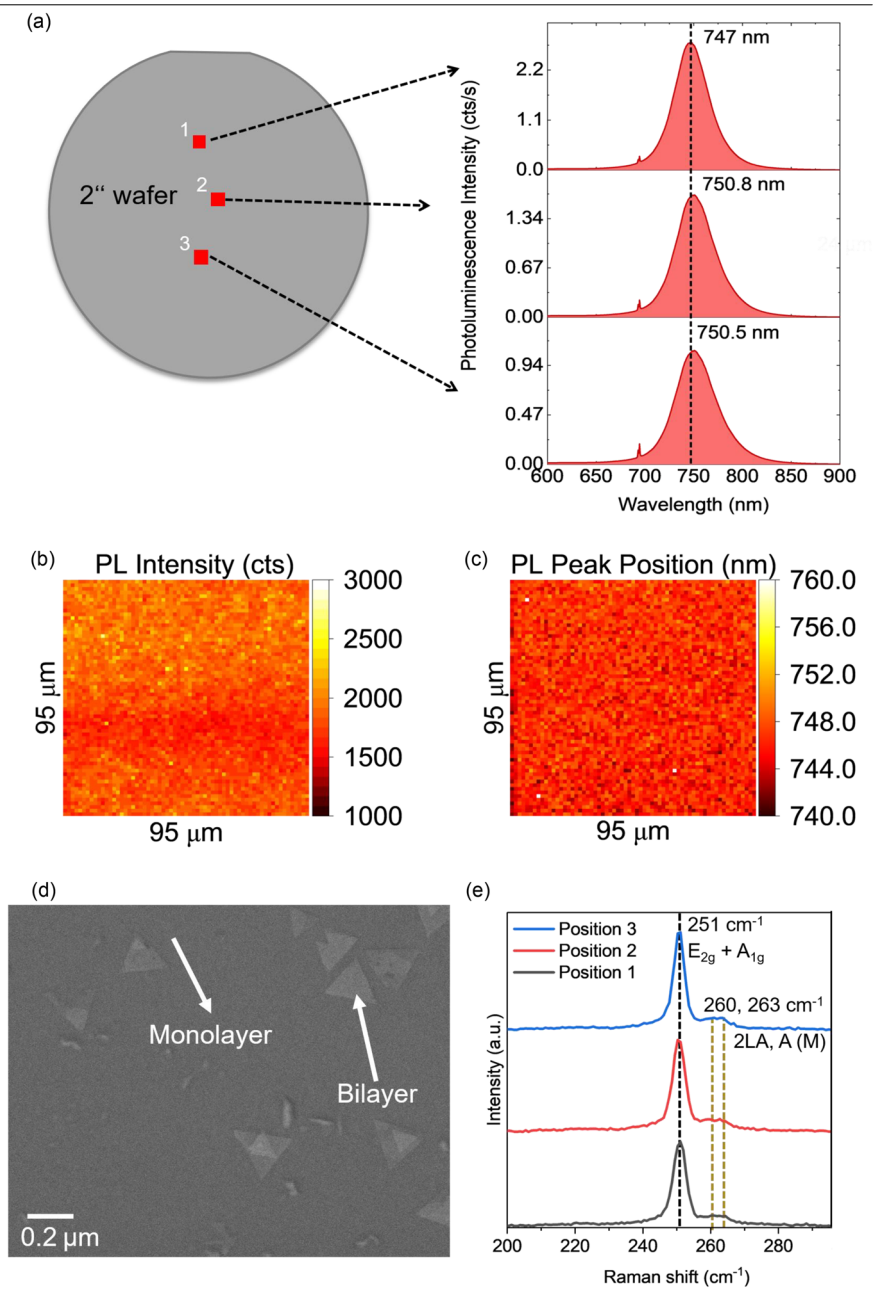


Fig. 1 | Homogeneity of the WSe_2 monolayer used in the 2D NIR LEDs. a Sketch of the 2-inch wafer showing areas where photoluminescence (PL) measurements were performed, with black arrows directed towards the corresponding PL spectrum. **b** PL intensity map over ~95 ×95 μm^2, **c** PL peak position map over ~95 ×95 μm^2, **d** SEM image of WSe_2 on sapphire showing areas with monolayer and bi-/multi-layers, and **e** Raman shift of WSe_2 at three different positions on the wafer.

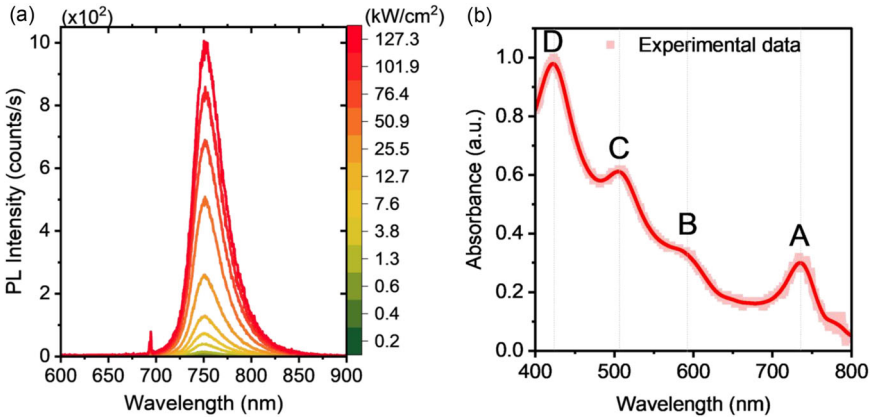


Fig. 2 | Excitonic signatures of WSe_2 monolayers used in the 2D NIR LEDs. a Excitation power-dependent PL emission of WSe_2 monolayers, **b** absorbance spectrum of monolayer WSe_2.

the WSe_2 monolayer shows a coverage of >98%, and an average peak position of 749 nm with a standard deviation of 3.6 nm. The corresponding average PL spectrum with the standard intensity deviation is given in Supplementary Fig. S1b.

Figure 1d shows a scanning electron microscopy (SEM) image of the coalesced WSe_2 film. A monolayer coverage of > 97% and contributions of bi-/multi-layers of less than 20% can be derived. The presence of bi-/multi-layers has been associated with the nucleation of new layers during the coalescence steps of the epitaxial monolayer, due to the limited migration length of surface adatoms on top of the already deposited monolayer[26]. To characterize the vibrational modes in these layers, Raman spectra were acquired at random spots in each of the three previously presented areas on the wafer. Figure 1e shows the Raman shift of WSe_2 at 251 cm^{-1}, representing the combination of the in-plane (E_{2g}) and out-of-plane (A_{1g}) normal modes, which have been reported to have the same frequency, thus cannot be separated[27]. The other signals around 260 and 263 cm^{-1} can be associated with the 2LA (M) mode, i.e., the overtone LA photon branch at the M point, and the A (M) mode, which indicates the presence of an active A-symmetry optical branch that exists due to structural disorder[27].

To shed more light on the excitonic signatures of monolayer WSe_2 on sapphire, excitation power-dependent steady–state PL measurements were carried out at room temperature. Figure 2a shows the evolution of PL spectrum as the excitation power density scales from 0.2 kW/cm^2 to 127 kW/cm^2. At the lowest excitation power, the emission peak is centered at 750.5 nm (see Supplementary Fig. S2) and can be attributed to the neutral A excitonic emission, which originates from the direct transition between the maximum of the valence band and the minimum of the conduction band at the K point in the band structure of WSe_2 monolayers[28]. This value agrees well with the already reported literature values for exfoliated[29,30], CVD[31], and MOCVD[25] -grown monolayer WSe_2. As the excitation power density increased to 127 kW/cm^2 the PL peak position is observed to slightly shift by ≤2 nm. This small shift implies no noticeable change in the emission mechanism, e.g., from neutral exciton to trion emission.

Figure 2b presents the optical absorption spectrum of the monolayer WSe_2, showing four visible excitonic transitions named A, B, C, and D at 735.5 nm, 591 nm, 507 nm, and 423.6 nm, respectively, in agreement with previously reported values for exfoliated[32] and MOCVD-grown WSe_2 monolayers[25]. The A peak is related to the exciton absorption at the direct bandgap at the K point, which agrees with previous reports[31,33]. The 15 nm Stokes shift between the absorption and the PL emission peak most likely originates from disorder in the monolayer, i.e. due to local variations of strain, doping or dielectric environment, and is typical for monolayer TMDCs[34]. The B absorption peak originates from the transition between the conduction band and the split-off valence band (VB), and agrees with the value reported by Aslan et al.[35]. The observed C and D absorption resonances have been related to an intralayer perturbation of the selenium (Se) p orbitals on the tungsten (W) d electron band[36,37] or to band nesting[38] which can initiate higher energy transitions closer to the Γ point.

Electroluminescence of large-area WSe_2-based LED devices

As the WSe_2 monolayer is shown to be rather homogeneous over a large area and exhibits the expected excitonic transitions, it can be embedded into a scalable LED architecture that allows for DC operation as depicted in Fig. 3a. On the anode side, a commercially obtained indium tin oxide (ITO) pre-patterned glass is used as a conductive substrate that facilitates outcoupling of the emitted photons. The hole transport layer and the electron blocking layer used are PEDOT: PSS and poly-TPD dissolved in chlorobenzene, respectively. The WSe_2 layer is transferred from the sapphire growth substrate onto the anode side of the device by a water-assisted method[39]. Customized commercial magnesium-doped zinc oxide quantum dots ($Mg_{0.2}Zn_{0.8}O$ QDs) dispersed in ethanol are spin-coated on top of the WSe_2 active layer and used as the electron-transport and hole-blocking layer on the cathode side. Aluminium is chosen as the metal contact and serves as a reflective mirror. All processes are beneficial for scalability and ease of integration.

To underline the expected device functionality, we show an energy level diagram following the well-known scheme from previous reports on 2D- and quantum dot LEDs[39,40]. The conduction band minimum (or LUMO) and valence band maximum energies (or HOMO) of PEDOT: PSS[41], and poly-TPD[42], as well as the work functions of ITO[43] and Al[44] have been taken from literature. The electron affinity and band gaps of both MgZnO[45] and WSe_2[46] were taken from the literature. The LED functionality thus relies on hole and electron injection into WSe_2 from the anode and cathode, respectively. The injected electrons (holes) are then effectively blocked by the energy barriers at the poly-TPD/WSe_2 (MgZnO/WSe_2) interfaces. The ~0.2 eV energy barrier between the conduction band minima of WSe_2 and MgZnO is expected to be overcome by electron flow when a small voltage is applied to the device.

Figure 3c shows the voltage-dependent electroluminescence (EL) spectra of the monolayer WSe_2-based NIR LED. The first observable NIR emission with a peak wavelength of 778 nm (see Supplementary Fig. S3) is observed at a voltage as low as 1.5 V, which we assign as the turn-on voltage. The intensity distribution of a 6 mm^2 large NIR LED biased by 4 V is shown in the inset. NIR emission is obvious from the whole defined active region. Increasing the bias voltage to 4 V resulted in higher peak EL intensity and a slightly red-shifted emission at 788 nm. Considering the EL peak positions, there are two main findings: first, a red shift is seen when comparing the minimum EL at 1.5 V with the PL emission of WSe_2 on the sapphire substrate (see Fig. 2a), and second, a gradual red shift of the EL peak energy is observed with increasing voltage.

To elucidate the origin of these shifts, the PL spectra of the WSe_2 monolayer are shown in Fig. 3d for different conditions after an excitation by a 532 nm laser. For as-grown conditions, the A exciton emission peak is

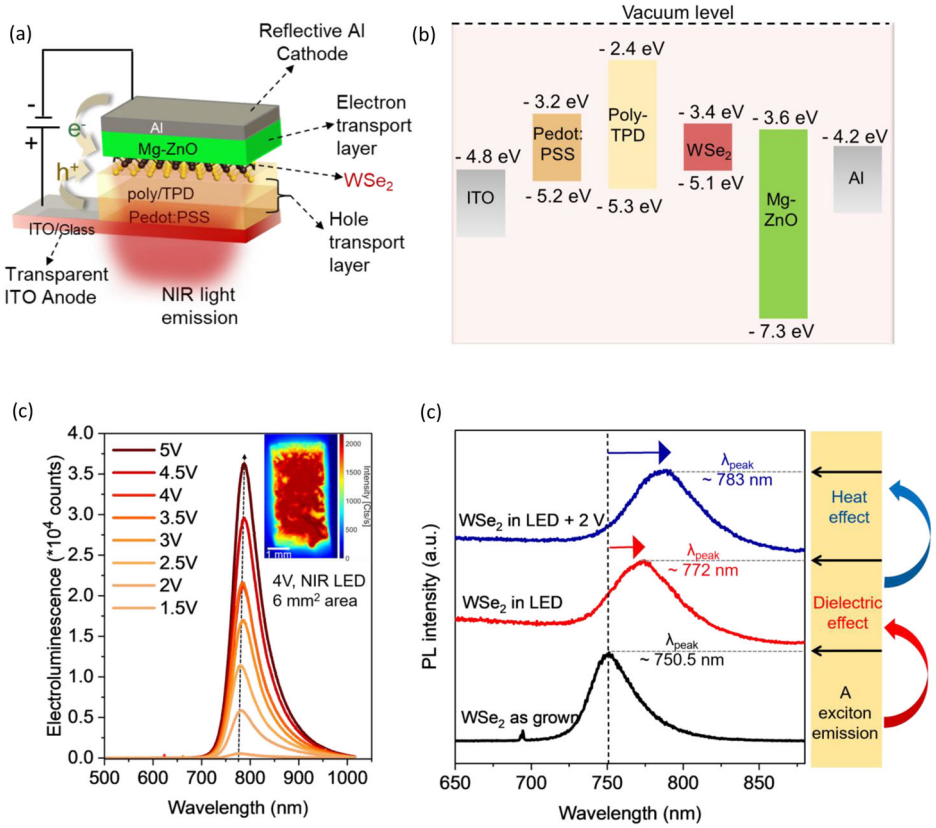


Fig. 3 | Architecture of scalable NIR LEDs based on monolayer WSe_2 and emission characteristics of WSe_2-based NIR LEDs. a Schematic drawing of the vertical LED architecture showing all layers included in the device, **b** Corresponding schematic band energy level diagram for anode layers, cathode layers, and the active WSe_2 monolayer, **c** Voltage-dependent electroluminescence spectra from the 2D NIR LED. Inset: image of the NIR emission at 4 V covering a 6 mm^2 area, and **d** PL of the as-grown WSe_2 on sapphire (black) compared with the PL of WSe_2 in the LED without applied voltage (red), and at 2 V (blue).

observed at 750.5 nm. However, the PL emission of the monolayer within the LED stack (the red spectrum) is shifted by ~21.5 nm, indicating the impact of the difference in the dielectric environment on the band gap of the active material[47]. In the initial case, the monolayer is underlaid by sapphire and uncapped (i.e., covered with air). In the latter case, the underlying substrate is changed to the aforementioned anode, i.e., TPD, and the monolayer is now capped by the cathode material, i.e., MgZnO. This difference can lead to an increased screening of the Coulomb interaction in the monolayer[48], reducing the band gap and the binding energy of the A exciton and causing a redshift in the peak wavelength. Additionally, the role of the quantum confined Stark effect caused by embedding the monolayer in the LED architecture can contribute to the shift in the monolayer emission in the device. The additional wavelength shift of about 11 nm observed with an applied voltage can be attributed to the expected heat effect on the active material (monolayer WSe_2) due to the current flow, which reduces the bandgap as formulated by O'Donnell et al.[49]. Note that the PL and EL peak position at a given applied bias voltage is similar (Supplementary Fig. S4), and no clear indication of trionic contributions is observed (see Supplementary Fig. S5). To verify the impact of Joule heating, the devices were operated in a pulsed mode (see Supplementary Fig. S6). Under pulsed excitation the EL peak shift with voltage is significantly reduced, e.g., to $\Delta\lambda = 5$ nm at 4 V compared to the large EL shift ($\Delta\lambda = 13$ nm) in the case of continuous excitation. This indicates that the Joule heating of the WSe_2 plays a significant role in the red shift observed in the voltage-dependent EL spectra in Fig. 3c, while other effects, such as carrier-density-dependent band gap renormalization[50] and band alignment-induced built-in electric fields at the interfaces[51], cannot be fully excluded.

Device performance and EQE analysis

After evaluating the emission characteristics of the NIR LED based on WSe_2 monolayers, the LED device performance was investigated. Figure 4a shows the current–voltage (I–V) characteristics with a rectifying behavior, consistent with the device architecture, where the active WSe_2 layer is embedded between a p-type hole transport layer (TPD) and a n-type electron transport layer (MgZnO). Rectifying ratios of 24 at ±3 V and 14.4 at ±2 V are obtained, and an onset voltage of ~1.5 V is observed, as shown in the inset. The I–V curve can be segmented into two parts: (1) The region at negative voltages below −1 V bias, where a small leakage current is observed, which can be due to defects in the device stack. (2) The forward bias region, where current is expected to flow, and a strong non-linear current increase with voltage is observed. The small deviation from an exponential curve at higher voltages is due to a series resistance, which may indicate a voltage drop across a resistive layer within the LED stack. As the voltage increases, the current rises, and the emitted light simultaneously becomes brighter (see Fig. 4b). As shown in the inset of Fig. 4b, the radiance becomes detectable at 1.5 V, corresponding to the onset voltage defined above. Actually, current literature shows higher values than in our device: In a DC-WSe_2 LED, a turn-on voltage (Vt) of 2.3 V for a device architecture based on exfoliated WSe_2 embedded into van der Waals heterostructures has been reported[52]. LEDs based on CVD-grown flakes and a waveguide-integrated structure[21] exhibit a Vt of 5 V, while AC-operated WSe_2 LEDs could be driven at a relatively low Vt of 2 V[23]. LEDs based on TMDCs with higher bandgap exhibit higher turn-on-voltages as expected: WS_2-based LEDs have been reported to have a Vt of 2.5–3 V[39,53], and for MoS_2-based LEDs, a Vt of close to 4 V[54] and 5 V[55], respectively, was shown.

By increasing the applied voltage, the radiance of the 6 mm^2 area emitting NIR LED further increases, reaching up to 2 μW cm^{-2} sr^{-1} at 5 V under DC operation, making it an improved performance compared to a large area CVD-based WSe_2 NIR LED, where an average radiance of 0.62 μW cm^{-2} sr^{-1} under AC-operation was reported[23]. Note that no further quantitative data on the radiance of WSe_2-LED are available from literature. Therefore, it is instructive to consider other TMDC-based LEDs: Here, a radiance of up to 1.1 μW cm^{-2} sr^{-1} at 7 V[39] and about 1 μW cm^{-2} sr^{-1} at 9 V[56] for large-area MOCVD-grown WS_2-based LEDs has been reported. For devices based on exfoliated WS_2, a significantly higher radiance of 60 μW cm^{-2} sr^{-1} could be obtained, but only from an area of μm size[57].

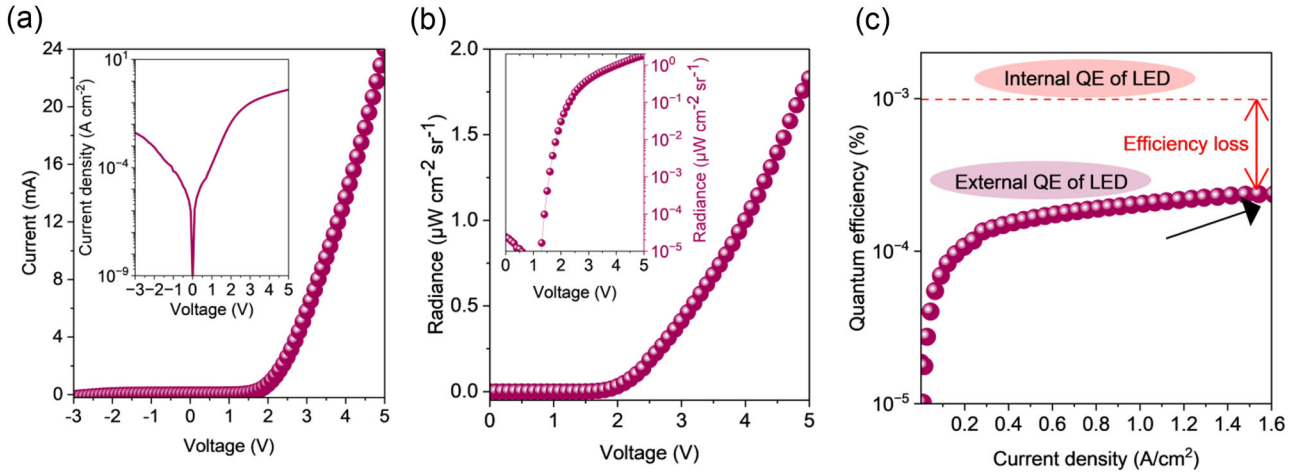


Fig. 4 | NIR LED device performance. a Current-voltage characteristics of the NIR LED. A semi-log scale of the *I–V* curve is shown in the inset to visualize the rectifying behavior of the device, **b** radiance versus voltage with the log scale in the inset, and **c** external quantum efficiency versus current density (purple symbols). The internal quantum efficiency IQE of the emitter measured on the growth substrate is indicated by the red dashed line.

The quantum efficiency versus current density curve is shown in Fig. 4c. An increasing external quantum efficiency (EQE), defined by the ratio of emitted photons to injected carriers, of the NIR LED is obtained as the current density increased, with an EQE of ~2.3×10^{-4}% at 1.6 A/cm^2, corresponding to a voltage of 5 V. In contrast to this, WSe_2 exfoliated flakes-based LEDs have been claimed to have EQEs ranging between 1%[58] and 8.4%[52,59]. Here, it must be noted that these devices are on a μm scale only and driven by very low currents. No radiance data are given. Considering other TMDC materials, an EQE of about 1×10^{-4}% was reported for large-area LEDs based on MOCVD-grown WS_2 monolayers[39], and values up to 1% for devices realized with CVD-grown WS_2[60] were given. In the latter case, however, no data on the radiance are provided. This value is orders of magnitude smaller than exfoliated flakes, which has been reported to be up to 8%[16].

The EQE is expressed by the product of the IQE, the extraction efficiency of emitted photons, η_{Ext}, and the injection efficiency η_{inj} of the carriers into the LED[61].

$$\mathrm{EQE} = \mathrm{IQE} \times \eta_{Ext} \times \eta_{inj} \tag{1}$$

This indicates that the low absolute EQE in our devices may be associated with several factors, including carrier injection, current leakage, light extraction, and the limited internal quantum efficiency (IQE) of the WSe_2. The IQE describes the ratio of photons generated inside the LED to the number of carriers that are injected into the active emitting layer[62]. For estimating the IQE of WSe_2 in the device, we first determined the photoluminescence quantum yield (QY) of WSe_2 on the sapphire growth substrate to be 1×10^{-3}% using a calibrated setup as described in the methods section. As no significant change in the PL intensity of the WSe_2 embedded in the completed device with respect to WSe_2 on sapphire was found (see Supplementary Fig. S7), the IQE in the device can be considered to be comparable to the QY of ~1×10^{-3}% measured on the sapphire growth substrate. This low IQE can be caused by higher defect densities in MOCVD-grown materials as compared to exfoliated flakes. These results suggest that the IQE of WSe_2 is a significant factor limiting the EQE in our devices, while other device-related factors may also contribute.

The ratio of EQE to IQE evaluated from Fig. 4c is given as 0.23. This difference can be attributed to a possible loss in the process of injection of carriers that recombine to generate photons, e.g. due to leakage currents, and/or for a limited extraction of light due to outcoupling losses. Therefore, this ratio is close to what can be expected for this geometry, considering all above limitations. Additionally, the turn on voltage of 1.5 V of this device is close to what can be expected from the bandgap of the WSe_2.

To gain further insight into the mechanism behind this limitation, the dependence of PL intensity, quantum yield (QY), and radiance of the NIR LED on the incident power density and generation rate, respectively, is discussed.

The relation between PL intensity I and excitation power density P, shown in Fig. 5a, follows the power law $I \propto P^k$ with a fitted slope of $k = 1$. This implies that despite the low QY of the material, the excitonic recombination mechanism remains unchanged over a wide range (more than three orders of magnitude) of excitation density[63]. To elaborate on the reason for this linearity, we applied the model suggested by Amani et al.[64] to investigate the dependence of the QY on optical generation rate, as given by Eq. (2),

$$QY = \frac{\tau_r^{-1}\langle N\rangle}{\tau_r^{-1}\langle N\rangle + B_{nr}n^2 + C_{bx}\langle N\rangle^2} \tag{2}$$

with the radiative lifetime τ_r, the nonradiative defect-mediated recombination rate B_{nr}, and the biexcitonic recombination coefficient C_{bx}. Figure 5b shows corresponding calculations, where, in a first approximation, the values $\tau_r = 0.3$ ns[65] and $C_{bx} = 0.05$ cm^2 s^{-1},[20] as given in literature for WSe_2 have been used. In this model, Shockley-Read-Hall losses are neglected, and we varied B_{nr} for illustration, as shown in Fig. 5b. When B_{nr} is set to 0 cm^2 s^{-1}, the generated excitons undergo fully radiative recombination at low generation rates, yielding a QY of 100%. At high generation rates, exciton-exciton annihilation can occur[16], leading to a QY droop as can be seen by the black dots. Increasing the nonradiative term to $B_{nr} = 1 \times 10^6$ cm^2 s^{-1} leads to two important findings. First, the overall QY is reduced and second, the onset of the exciton-exciton annihilation (EEA) is shifted towards higher generation rates.

We now consider that the QY of 1×10^{-3}% for the as-grown sample was measured at a generation rate of 1.7×10^{21} cm^{-2} s^{-1}. Using this QY value for calibration, we extracted the QY for the whole power series presented in Fig. 5a and added the data to Fig. 5b as green balls. As can be seen, the QY of ~1×10^{-3}% is virtually constant over the measured generation rate range of 2.6×10^{19}…1.7×10^{22} cm^{-2} s^{-1}. This value, together with the above given literature data for the radiative lifetime and the biexcitonic recombination coefficient, was used to derive $B_{nr} = 1 \times 10^9$ cm^2 s^{-1} (red circles). No visible QY droop was observed, indicating that EEA may be negligible within the experimentally accessed generation-rate range. Note that the onset of the QY droop depends on the exact values of τ_r and C_{bx} (see Supplementary Fig. S8), which, however, cannot be extracted from our data.

We introduce this knowledge to elucidate the dependence of the emitted NIR light on the generation rate as shown in Fig. 5c. The optical and

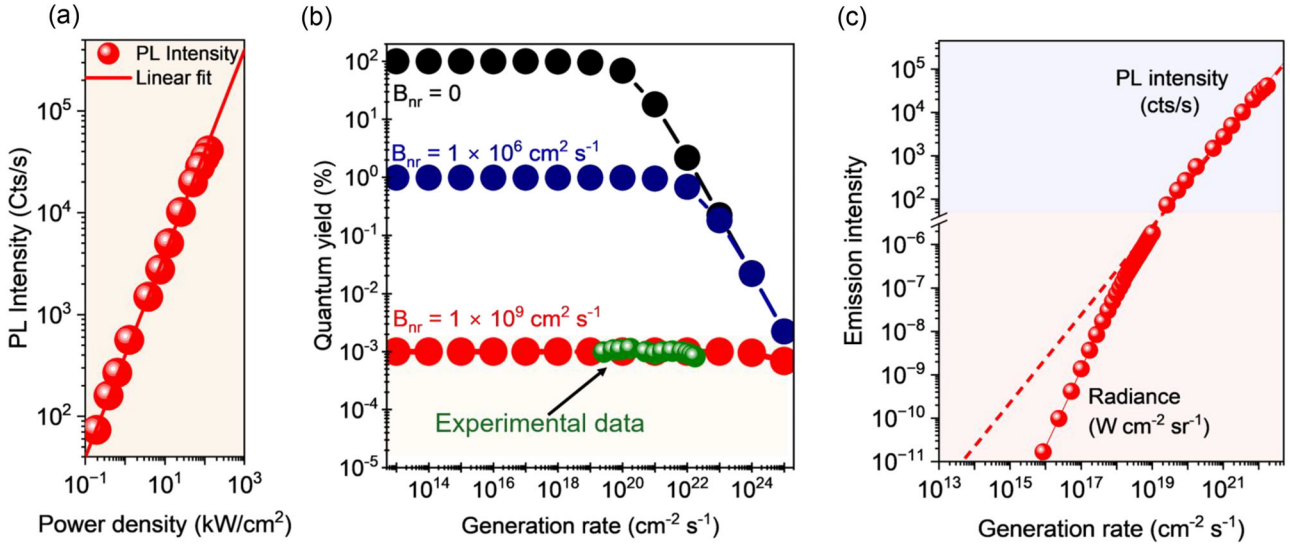


Fig. 5 | Mechanism of EQE limitations in the WSe_2-based NIR LEDs. a Relation between excitation power density and PL intensity for WSe_2 on sapphire on a log-log scale showing the linearity of the PL emission over more than 3 orders of magnitude, **b** generation rate dependence of the quantum yield (QY) for different nonradiative defect-mediated recombination rates $B_{nr} = 0$ (black dots), 1×10^6 cm^2 s^{-1} (blue dots), and 1×10^9 cm^2 s^{-1} (red dots). The green balls represent data from the power-dependent PL studies presented in (**a**), and **c** combined graph of both the NIR LED radiance (red shaded area) of the device and the WSe_2 PL intensity measured on the growth substrate (blue shaded area) vs. generation rate. The dashed line is a power law guided line with a fixed slope of 1.

electrical photon generation rates were calculated following an identical approach as introduced by Uddin et al.[66]. The optical generation rate, G, is determined based on the following relation,

$$G = \frac{aP}{hv} cm^{-2}s^{-1} \quad (3)$$

where P is the laser power density, A is the area of the laser spot, a is the absorbance at the incident photon wavelength in percent, and hv is the incident photon energy at 532 nm.

The electrical generation rate, Gv, in the LED is determined by the following relation,

$$Gv = \frac{j}{e} cm^{-2}s^{-1} \quad (4)$$

where j is the current density and e is the elementary charge.

Figure 5c shows a combined plot of the PL intensity of the WSe_2 on sapphire and the radiance of the NIR LED as a function of generation rate. The PL intensity (blue shaded area), mainly studied for high generation rates for experimental reasons, clearly follows the dashed line with a slope of 1, indicating an unchanged recombination mechanism, as discussed already above. No clear impact of exciton-exciton annihilation at high excitation densities is observed which we attribute to the overall low QY of the MOCVD-grown material, i.e. the high value of B_{nr}, as depicted in Fig. 5b. Additionally, strain may lead to a reduced exciton-exciton annihilation at high generation rates as reported in literature[66].

Conversely, although the radiance versus electrical generation rate (red-shaded area) also follows the dashed line at high generation rates, a deviation is observed at lower generation rates. This deviation, in which the radiance increases super-linearly with generation rate, can indicate Shockley-Read-Hall recombination processes in the LED at low carrier concentrations or can be due to leakage currents as discussed in Fig. 4.

In conclusion, we present near-infrared light-emitting device performance based on scalable MOCVD-grown WSe_2 monolayers using a vertical device architecture. We demonstrated the monolayer's homogeneity on a wafer scale using PL maps that showed uniform WSe_2 PL signals and the corresponding peak positions at 749 nm, with a standard deviation of 2 nm at room temperature. We confirmed the dominance of excitonic band-to-band transitions for monolayers. The monolayer was successfully embedded in a 6 mm^2-scale vertical LED architecture using PEDOT: PSS and poly-TPD as the anode and Mg-doped ZnO as the cathode. Upon applying a forward bias to the device, a near-infrared emission at 778 nm was observed at 1.5 V, and the intensity increased with increasing bias. As a consequence of the band alignment in our vertical device architecture, the devices showed a rectifying I–V curve with an onset voltage of ~1.5 V and a rectifying ratio of 24 at ±3 V. A NIR emission radiance of 2 μW cm^{-2} sr^{-1} is obtained at 5 V. While several factors, such as carrier injection, current leakage and light extraction, may limit the EQE of the LED, we demonstrate that the low IQE of the MOCVD-grown WSe_2 due to nonradiative defect-mediated recombination is a significant factor. This leaves the further improvement of growth and post-processing of MOCVD-grown WSe_2 monolayers as one key issue towards achieving scalable NIR LEDs that potentially may suit applications in biomedical diagnostic imaging.

Methods

Monolayer WSe_2 growth

A water-assisted growth process was developed in a commercial AIXTRON close-coupled showerhead (CCS) reactor with a capacity for 7 × 2-inch substrates. A 2-inch c-plane (0001) sapphire with an offcut of 0.2–0.25° normal to the m-plane was used as the substrate for this growth process. Prior to the start of the growth process, the sapphire was annealed at 1050 °C for 30 min in a hydrogen gas atmosphere at a pressure of 150 hectopascal (hPa). The precursors used for WSe_2 deposition are commercial $W(CO)_6$ (tungsten hexacarbonyl, 99.99%) and $C_6H_{14}Se$ (di-iso-propyl selenide (DiPSe), 99.999%) for W and Se, respectively. H_2O (99.9999%) was injected as an additive during growth, and purified H_2 was used as the carrier gas. After the substrate annealing step, the growth process consists of the nucleation phase for 8 min at 720 °C with the introduction of $W(CO)_6$ and $C_6H_{14}Se$, the lateral growth phase for 10 min at 820 °C, and a W precursor ramp-down phase with 50 nmol/min H_2O flux for 19 min, resulting in the fully coalesced WSe_2 layer. A detailed description of the growth mechanism and MOCVD process has been reported by Wang et al.[24].

LED fabrication

A 150 nm thick ITO film with sheet resistance of 15 ohms/sq and average surface roughness of 1 nm, pre-patterned on 1.5 × 1.5 cm^2 large glass was

purchased from Vision Tec Systems Ltd and used as the transparent substrate. The PEDOT: PSS and poly-TPD used together with the patterned glass as the anode were purchased from Sigma Aldrich and Solaris Chem Inc., respectively. The substrate was first cleaned by the standard cleaning process, including a 10-min oxygen plasma treatment. Then, the PEDOT: PSS was spin-coated at 2000 rpm for 60 s and post-annealed on hot plate in air for 20 min at 150 °C. The pre-dissolved poly-TPD flakes in chlorobenzene with a 1.5 g/ml concentration was spin-coated on the PEDOT: PSS film at 2000 rpm for 30 s and post-annealed in air for 30 min at 150 °C. The monolayer WSe_2 was transferred from sapphire onto the poly-TPD surface with the aid of a 0.09 mg/mL toluene solution of polystyrene and water. The monolayer with PS on poly-TPD was post-heated in air using a two-step process: (1) Heating at 90 °C for 30 min to slowly evaporate the solvent remains and completely dry up the remaining water content that was not dried by nitrogen. At this stage, wrinkles caused by the transfer process are clearly visible; hence, the next step. (2) The heating temperature was ramped up to 150 °C and left for 1 h to enhance the adhesion between the monolayer and poly-TPD, and to remove the wrinkles. This ensures good interlayer coupling, which is eventually important for homogeneous device emission and carrier injection. To effectively remove the PS, the device was immersed in toluene for 10 min and carefully dried out with nitrogen. To complete the device stack, a commercial 20% Mg-doped ZnO QD dispersed in ethanol (supplied by Avantama) was spin-coated at 2000 rpm for 50 s and post-annealed at 120 °C for exactly 20 min. After that, 200 nm aluminium cathode contacts were evaporated using a pre-patterned metal mask and an electron-beam evaporation method below 3×10^{-6} mbar vacuum pressure.

Characterization techniques

For all PL, Raman spectra and PL maps, a confocal NT-MDT NTEGRA Spectra setup was used. Sample excitation was done with 532 nm wavelength, using a solid-state laser with a spot size of ~1.5 µm and a 100× objective. The voltage-dependent PL measurement was also performed using this setup, with an additional Keithley 2612 source meter as the voltage source. The absorption spectra were recorded using the Shimadzu UV-Vis absorption spectrometer UV-2550. To account for the correct absorption by the monolayer, the spectra were corrected by subtracting a sapphire reference spectrum from it. EL spectra were taken using both the NT-MDT NTEGRA and a home-built setup based on a 600 nm long-pass filter from Thorlabs, an iHR 320 monochromator from HORIBA synced with a nitrogen-cooled Jobin Yvon Symphony-Solo Detector CCD. For the quantum yield measurement, an integrating sphere with the home-built PL setup together with the NTEGRA was used. The quantum yield of the reference sample on sapphire (cadmium selenide (CdSe) quantum dots (QDs)) was first measured. Then, the PL of both the reference CdSe sample and the WSe_2 monolayer on sapphire was measured under the same conditions. Lastly, the QY, defined as the ratio of emitted to absorbed photons, was calculated using both the integrated PL counts and the absorbance at the excitation wavelength of 532 nm. For the scanning electron microscope (SEM), the monolayer on sapphire was properly grounded and imaged with a Zeiss REM Supra25 at an accelerating voltage of 2 kV, using the secondary electron detection mode. The bias voltage-dependent radiance measurement was done with a Keithley 2601 source meter connected to a calibrated Si-photodiode (Newport Sensor 818-UV), which is controlled by custom-made LabVIEW software. The same setup consisting of the Keithley 2601 source meter and the LabVIEW software was used to obtain current-voltage (*I–V)* characteristics of the LEDs.

Data availability

The datasets generated and/or analyzed during the current study are available in the TUDOdata repository, https://doi.org/10.71955/DUEDATA-2026-H1ZPDB.

Received: 9 March 2026; Accepted: 15 September 2026;
Published online: 30 September 2026

References

1. Liu, G. et al. Laser-driven broadband near-infrared light source with watt-level output. *Nat. Photon.* **18**, 562–568 (2024).
2. Farber, C., Mahnke, M., Sanchez, L. & Kurouski, D. Advanced spectroscopic techniques for plant disease diagnostics. A review. *TrAC Trends Anal. Chem.* **118**, 43–49 (2019).
3. Mahlein, A.-K., Oerke, E.-C., Steiner, U. & Dehne, H.-W. Recent advances in sensing plant diseases for precision crop protection. *Eur. J. Plant Pathol.* **133**, 197–209 (2012).
4. Wang, Y.-J. et al. Qualitative and quantitative diagnosis of nitrogen nutrition of tea plants under field condition using hyperspectral imaging coupled with chemometrics. *J. Sci. Food Agric.* **100**, 161–167 (2020).
5. Ali, M. M. et al. Non-destructive techniques of detecting plant diseases: A review. *Physiol. Mol. Plant Pathol.* **108**, 101426 (2019).
6. Allen, P. M. et al. InAs(ZnCdS) Quantum Dots Optimized for Biological Imaging in the Near-Infrared. *J. Am. Chem. Soc.* **132**, 470–471 (2010).
7. Lu, H., Carroll, G. M., Neale, N. R. & Beard, M. C. Infrared Quantum Dots: Progress, Challenges, and Opportunities. *ACS Nano* **13**, 939–953 (2019).
8. Dimakis, E. et al. Coaxial Multishell (In,Ga)As/GaAs Nanowires for Near-Infrared Emission on Si Substrates. *Nano Lett.* **14**, 2604–2609 (2014).
9. Svensson, C. P. T. et al. Monolithic GaAs/InGaP nanowire light emitting diodes on silicon. *Nanotechnology* **19**, 305201 (2008).
10. Broell, M. et al. New developments on high-efficiency infrared and InGaAlP light-emitting diodes at OSRAM Opto Semiconductors. In *Light-Emitting Diodes: Materials, Devices, and Applications for Solid State Lighting XVIII* vol. 9003, 42–47 (SPIE, 2014).
11. Vasilopoulou, M. et al. Advances in solution-processed near-infrared light-emitting diodes. *Nat. Photon.* **15**, 656–669 (2021).
12. Zhao, X. et al. Recent Progress in Long-Wavelength InGaN Light-Emitting Diodes from the Perspective of Epitaxial Structure. *Adv. Photonics Res.* **4**, 2300061 (2023).
13. Eichfeld, S. M. et al. Highly Scalable, Atomically Thin WSe_2 Grown via Metal–Organic Chemical Vapor Deposition. *ACS Nano* **9**, 2080–2087 (2015).
14. Iff, O. et al. Strain-Tunable Single Photon Sources in WSe_2 Monolayers. *Nano Lett.* **19**, 6931–6936 (2019).
15. Kim, H., Moon, J. S., Noh, G., Lee, J. & Kim, J.-H. Position and Frequency Control of Strain-Induced Quantum Emitters in WSe_2 Monolayers. *Nano Lett.* **19**, 7534–7539 (2019).
16. Lien, D.-H. et al. Electrical suppression of all nonradiative recombination pathways in monolayer semiconductors. *Science* **364**, 468–471 (2019).
17. Tebyetekerwa, M. et al. Mechanisms and Applications of Steady-State Photoluminescence Spectroscopy in Two-Dimensional Transition-Metal Dichalcogenides. *ACS Nano* **14**, 14579–14604 (2020).
18. Withers, F. et al. WSe_2 Light-Emitting Tunneling Transistors with Enhanced Brightness at Room Temperature. *Nano Lett.* **15**, 8223–8228 (2015).
19. Khelifa, R. et al. WSe_2 Light-Emitting Device Coupled to an h-BN Waveguide. *ACS Photonics* **10**, 1328–1333 (2023).
20. Kim, H. et al. Synthetic WSe_2 monolayers with high photoluminescence quantum yield. *Sci. Adv.* **5**, eaau4728 (2019).
21. Yang, X. et al. A Waveguide-Integrated Two-Dimensional Light-Emitting Diode Based on p-Type WSe_2/n-Type CdS Nanoribbon Heterojunction. *ACS Nano* **16**, 4371–4378 (2022).
22. Liu, C.-H. et al. Nanocavity Integrated van der Waals Heterostructure Light-Emitting Tunneling Diode. *Nano Lett.* **17**, 200–205 (2017).
23. Lien, D.-H. et al. Large-area and bright pulsed electroluminescence in monolayer semiconductors. *Nat. Commun.* **9**, 1229 (2018).
24. Wang, Y. et al. Water-assisted multistep MOCVD for wafer-scale layer-by-layer growth of WSe_2. *MRS Bull.* **50**, 1283–1295 (2025).

25. Choudhury, T. H. et al. Comparison of the MOCVD growth and properties of wafer-scale transition metal dichalcogenide epitaxial monolayers. *2D Mater.* **12**, 045009 (2025).
26. Zhang, X. et al. Diffusion-Controlled Epitaxy of Large Area Coalesced WSe_2 Monolayers on Sapphire. *Nano Lett.* **18**, 1049–1056 (2018).
27. del Corro, E. et al. Excited Excitonic States in 1L, 2L, 3L, and Bulk WSe_2 Observed by Resonant Raman Spectroscopy. *ACS Nano* **8**, 9629–9635 (2014).
28. Kaplan, D. et al. Excitation intensity dependence of photoluminescence from monolayers of MoS_2 and WS_2 /MoS_2 heterostructures. *2D Mater.* **3**, 015005 (2016).
29. Desai, S. B. et al. Strain-Induced Indirect to Direct Bandgap Transition in Multilayer WSe_2. *Nano Lett.* **14**, 4592–4597 (2014).
30. Andres-Penares, D. et al. Out-of-plane trion emission in monolayer WSe_2 revealed by whispering gallery modes of dielectric microresonators. *Commun. Mater.* **2**, 52 (2021).
31. Ahn, G. H. et al. Strain-engineered growth of two-dimensional materials. *Nat. Commun.* **8**, 608 (2017).
32. Pan, Y. et al. Exciton tuning in monolayer WSe_2 via substrate induced electron doping. *Nanosc. Adv.* **4**, 5102–5108 (2022).
33. Huang, J.-K. et al. Large-Area Synthesis of Highly Crystalline WSe_2 Monolayers and Device Applications. *ACS Nano* **8**, 923–930 (2014).
34. Kolesnichenko, P. V. et al. Disentangling the effects of doping, strain and disorder in monolayer WS_2 by optical spectroscopy. *2D Mater.* **7**, 025008 (2020).
35. Aslan, B., Deng, M. & Heinz, T. F. Strain tuning of excitons in monolayer WSe_2. *Phys. Rev. B* **98**, 115308 (2018).
36. Beal, A. R., Knights, J. C. & Liang, W. Y. Transmission spectra of some transition metal dichalcogenides. II. Group VIA: trigonal prismatic coordination. *J. Phys. C Solid State Phys.* **5**, 3540–3551 (1972).
37. Zhao, W. et al. Evolution of Electronic Structure in Atomically Thin Sheets of WS_2 and WSe_2. *ACS Nano* **7**, 791–797 (2013).
38. Eroglu, Z. E. et al. Filling Exciton Trap-States in Two-Dimensional Tungsten Disulfide (WS_2) and Diselenide (WSe_2) Monolayers. *Nanomaterials* **11**, 770 (2021).
39. Andrzejewski, D. et al. Scalable Large-Area p–i–n Light-Emitting Diodes Based on WS_2 Monolayers Grown via MOCVD. *ACS Photonics* **6**, 1832–1839 (2019).
40. Jang, E. & Jang, H. Review: Quantum Dot Light-Emitting Diodes. *Chem. Rev.* **123**, 4663–4692 (2023).
41. Wepfer, S. et al. Solution-Processed CuInS2-Based White QD-LEDs with Mixed Active Layer Architecture. *ACS Appl. Mater. Interfaces* **9**, 11224–11230 (2017).
42. Bae, W. K. et al. Highly Efficient Green-Light-Emitting Diodes Based on CdSe@ZnS Quantum Dots with a Chemical-Composition Gradient. *Adv. Mater.* **21**, 1690–1694 (2009).
43. Raj, V. et al. Passivation of InP solar cells using large area hexagonal-BN layers. *npj 2D Mater. Appl* **5**, 12 (2021).
44. Kondo, S. et al. Organic thermoelectric device utilizing charge transfer interface as the charge generation by harvesting thermal energy. *Nat. Commun.* **15**, 8115 (2024).
45. Giri, P. MgZnO Nanoparticle-Based Metal–Semiconductor–Metal UV Photodetector. *J. Electron. Mater.* **51**, 1866–1875 (2022).
46. Kim, H. & Choi, H. J. Thickness dependence of work function, ionization energy, and electron affinity of Mo and W dichalcogenides from DFT and GW calculations. *Phys. Rev. B* **103**, 085404 (2021).
47. Buscema, M., Steele, G. A., Van Der Zant, H. S. J. & Castellanos-Gomez, A. The effect of the substrate on the Raman and photoluminescence emission of single-layer MoS_2. *Nano Res.* **7**, 561–571 (2014).
48. Raja, A. et al. Coulomb engineering of the bandgap and excitons in two-dimensional materials. *Nat. Commun.* **8**, 15251 (2017).
49. O'Donnell, K. P. & Chen, X. Temperature dependence of semiconductor band gaps. *Appl. Phys. Lett.* **58**, 2924–2926 (1991).
50. Park, Y. et al. Interplay between many body effects and Coulomb screening in the optical bandgap of atomically thin MoS_2. *Nanoscale* **9**, 10647–10652 (2017).
51. Liu, T., He, M., Shen, C., Xia, C. & Li, X. Interface-controlled band alignments in Janus Ga2STe/MoSi2N4 vdWHs. *Phys. B Condens. Matter* **666**, 415061 (2023).
52. Withers, F. et al. Light-emitting diodes by band-structure engineering in van der Waals heterostructures. *Nat. Mater.* **14**, 301–306 (2015).
53. Ahmed, T. et al. Bright and Efficient Light-Emitting Devices Based on 2D Transition Metal Dichalcogenides. *Adv. Mater.* **35**, 2208054 (2023).
54. Im, H., Kim, J., Kim, J. & Kim, S. Scalable Bilayer MoS_2-Based Vertically Inverted p–i–n Light-Emitting Diodes. *Adv. Mater. Interfaces* **11**, 2300319 (2024).
55. Rangnekar, S. V. et al. Electroluminescence from Megasonically Solution-Processed MoS_2 Nanosheet Films. *ACS Nano* **17**, 17516–17526 (2023).
56. Andrzejewski, D. et al. Flexible Large-Area Light-Emitting Devices Based on WS_2 Monolayers. *Adv. Optical Mater.* **8**, 2000694 (2020).
57. Andrzejewski, D., Hopmann, E., John, M., Kümmell, T. & Bacher, G. WS_2 monolayer-based light-emitting devices in a vertical p–n architecture. *Nanoscale* **11**, 8372–8379 (2019).
58. Wang, S. et al. Efficient Carrier-to-Exciton Conversion in Field Emission Tunnel Diodes Based on MIS-Type van der Waals Heterostack. *Nano Lett.* **17**, 5156–5162 (2017).
59. Wang, J., Verzhbitskiy, I. & Eda, G. Electroluminescent Devices Based on 2D Semiconducting Transition Metal Dichalcogenides. *Adv. Mater.* **30**, 1802687 (2018).
60. Kim, J. et al. Large-Area Organic–Transition Metal Dichalcogenide Hybrid Light-Emitting Device. *ACS Photonics* **8**, 1152–1158 (2021).
61. Zhao, H., Liu, G., Zhang, J., Arif, R. A. & Tansu, N. Analysis of Internal Quantum Efficiency and Current Injection Efficiency in III-Nitride Light-Emitting Diodes. *J. Disp. Technol.* **9**, 212–225 (2013).
62. Li, B. et al. Advances in understanding quantum dot light-emitting diodes. *Nat. Rev. Electr. Eng.* **1**, 412–425 (2024).
63. Guerra Davila, Y. et al. Temperature and power-dependent photoluminescence spectroscopy in suspended WSe_2 monolayer. *J. Phys. D Appl. Phys.* **57**, 165304 (2024).
64. Amani, M. et al. Near-unity photoluminescence quantum yield in MoS_2. *Science* **350**, 1065–1068 (2015).
65. Palummo, M., Bernardi, M. & Grossman, J. C. Exciton Radiative Lifetimes in Two-Dimensional Transition Metal Dichalcogenides. *Nano Lett.* **15**, 2794–2800 (2015).
66. Uddin, S. Z., Higashitarumizu, N., Kim, H., Rahman, I. K. M. R. & Javey, A. Efficiency Roll-Off Free Electroluminescence from Monolayer WSe_2. *Nano Lett.* **22**, 5316–5321 (2022).

Acknowledgements

The Authors thank J. Korte for technical support in acquiring the inset of Fig. 3c.

Author contributions

T.F: Device fabrication, optical, and electrical characterization, data analysis and visualization, writing, and editing. M.K: Device characterization, data collection, and data analysis. S.T: MOCVD process development, TMDC characterization, and corresponding data analysis. H.M: Optical data modeling. N.S: Scanning electron microscopy imaging of monolayers. Y.W: MOCVD process development, TMDC characterization, and corresponding data analysis. Y.D: MOCVD process development, TMDC characterization, and corresponding data analysis. M.H: Supervision and MOCVD hardware development. H.K: MOCVD process conception and supervision. A.V: MOCVD process conception, supervision, and review. T.K: Conception, writing, review and editing, scientific discussion, and supervision. G.B: Conception, supervision, review, editing, and scientific discussion. All authors reviewed the manuscript.

Funding
This study was funded by Deutsche Forschungsgemeinschaft (DFG, German Research Foundation) – project IRTG 2803 – 461605777 and projects BA 1422/21-2 and VE 597/5-2. The funder played no role in study design, data collection, analysis and interpretation of data, or the writing of this manuscript. Open Access funding enabled and organized by Projekt DEAL.

Competing interests
The authors declare no competing interests.

Additional information
Supplementary information The online version contains supplementary material available at https://doi.org/10.1038/s41699-026-00745-7.

Correspondence and requests for materials should be addressed to Tilmar Kümmell.

Reprints and permissions information is available at http://www.nature.com/reprints

Publisher's note Springer Nature remains neutral with regard to jurisdictional claims in published maps and institutional affiliations.

Open Access This article is licensed under a Creative Commons Attribution 4.0 International License, which permits use, sharing, adaptation, distribution and reproduction in any medium or format, as long as you give appropriate credit to the original author(s) and the source, provide a link to the Creative Commons licence, and indicate if changes were made. The images or other third party material in this article are included in the article's Creative Commons licence, unless indicated otherwise in a credit line to the material. If material is not included in the article's Creative Commons licence and your intended use is not permitted by statutory regulation or exceeds the permitted use, you will need to obtain permission directly from the copyright holder. To view a copy of this licence, visit http://creativecommons.org/licenses/by/4.0/.

© The Author(s) 2026